

Article

Spatial and Temporal Distribution of Northwest Cape Transmitter (19.8 kHz) Radio Signals Using Data Collected by the China Seismo-Electromagnetic Satellite

Honggeng Cai ^{1,2,3,4}, Shufan Zhao ^{2,3,*}, Li Liao ⁵ , Xuhui Shen ^{2,3,*} and Hengxin Lu ⁴

¹ School of Emergency Management Science and Engineering, University of Chinese Academy of Sciences, Beijing 100049, China; caihonggeng21@mailsucas.ac.cn

² State Key Laboratory of Space Weather, National Space Science Center, Chinese Academy of Sciences, Beijing 100190, China

³ Key Laboratory of Solar Activity and Space Weather, National Space Science Center, Chinese Academy of Sciences, Beijing 100190, China

⁴ National Institute of Natural Hazards, Ministry of Emergency Management of China, Beijing 100085, China; hengxinlu@ninhm.ac.cn

⁵ Institute of Geophysics, China Earthquake Administration, Beijing 100081, China; liaoli@cea-igp.ac.cn

* Correspondence: zhaoshufan@nssc.ac.cn (S.Z.); shenxuhui@nssc.ac.cn (X.S.)

Abstract: Very Low Frequency (VLF) waves radiated from ground-based transmitters are crucial for long-distance communication and underwater navigation. These waves can reflect between the Earth's surface and the ionosphere for Earth-ionosphere waveguide propagation. Additionally, they can penetrate not only the ionosphere but also the magnetosphere, where they interact with high-energy particles in the radiation belt. Therefore, studying the spatial and temporal distribution of VLF radio signals holds significant importance. Such research enables us to understand the propagation characteristics of VLF signals, their interaction with radiation belt particles, and their response to space weather and lithospheric activity events. In this paper, we investigate the seasonal variations in the intensity of the Northwest Cape (NWC) transmitter (19.8 kHz) radio signals at satellite altitude and the displacement of the electric field's peak center. Our analysis is based on the nightly China Seismo-Electromagnetic Satellite (CSES) data from 2019 to 2021. The results reveal the following: (1) There is no significant seasonal variation in the electric field strength within a small area (2.5° radius) around the NWC transmitter. However, a clear seasonal variation in the electric field strength is observed within a larger area (15° radius), with higher strength during winter compared with summer. (2) The power spectral density of the electric field remains constant within the peak central area (approximately 1~2° radius), but it decays with distance outside this region, showing a north-south asymmetry. Moreover, the decay rate of the radiation electric field is slower in the northern direction than in the southern direction. (3) The center of the electric field moves northward from summer to winter and southward from winter to summer. (4) In winter, VLF waves radiated by the NWC transmitter may predominantly propagate by being ducted toward the conjugate hemisphere.

Keywords: NWC transmitter; CSES; strength of electric field; VLF radio signals; spatial and temporal distribution



Citation: Cai, H.; Zhao, S.; Liao, L.; Shen, X.; Lu, H. Spatial and Temporal Distribution of Northwest Cape Transmitter (19.8 kHz) Radio Signals Using Data Collected by the China Seismo-Electromagnetic Satellite. *Atmosphere* **2023**, *14*, 1816. <https://doi.org/10.3390/atmos14121816>

Academic Editor: Masashi Hayakawa

Received: 19 November 2023

Revised: 8 December 2023

Accepted: 11 December 2023

Published: 13 December 2023



Copyright: © 2023 by the authors. Licensee MDPI, Basel, Switzerland. This article is an open access article distributed under the terms and conditions of the Creative Commons Attribution (CC BY) license (<https://creativecommons.org/licenses/by/4.0/>).

1. Introduction

Ground-based Very Low Frequency (VLF) waves, typically in the 10–30 kHz range, can propagate back and forth between the Earth's surface and the ionosphere and travel long distances via the Earth-ionosphere waveguide (EIWG). During propagation, some of the wave's energy can penetrate the ionosphere and propagate in a right-hand circularly polarized whistler mode toward the top of the ionosphere and into the magnetosphere. Satellites can receive these signals [1]. However, when VLF waves penetrate the D/E

region of the ionosphere, their energy is absorbed due to intense collisions. Still, some energy can pass through the ionosphere and reach the magnetosphere. Here, the VLF wave undergoes cyclotron resonance with electrons, leading to their precipitation. This process is one of the mechanisms that cause the slow loss of energetic electrons in the radiation belts [2–5]. Recent studies indicate that electron precipitation in the outer radiation belts is primarily caused by chorus waves, lightning whistles, plasma hiss, and ground-based VLF transmitter signals. Among these, the VLF waves radiated by the Northwest Cape (NWC) transmitter located in Australia have a significant impact on electron precipitation in the inner radiation belts at 100–400 keV and 500–800 keV [6–12].

Numerous studies have demonstrated that the primary energy attenuation for upward propagation of VLF waves occurs in the low ionosphere region. After passing through the low ionosphere, the energy of these waves hardly attenuates [13–16]. The low ionosphere is mainly affected by solar extreme ultraviolet radiation, which exhibits significant seasonal, diurnal, and 27-day cyclic variations [17–20]. Additionally, it is subject to changes from solar flare activity, atmospheric effects (such as lightning and aerosols), precipitation of high-energy particles in the magnetosphere, and lithospheric activity (such as earthquakes) [21–25]. Accordingly, variations in the low ionosphere directly affect the spatial and temporal distribution of VLF radio signals penetrating the ionosphere. To quantitatively study the influence of the low ionosphere on VLF waves propagating through the ionosphere, Cohen et al. (2012) [26] statistically analyzed the radiated energy distribution at satellite altitudes over 16 ground-based VLF transmitters, such as the NWC and the NAA transmitters, as well as over the magneto conjugate region, using six years of electromagnetic field data from the DEMETER satellite. They estimated the energy of ground-based VLF transmitters reaching the top of the ionosphere and investigated the dependence of the VLF radio signals on solar activity and geomagnetism at a range of 150 km for a period of six years. Němec et al. (2020) [12] comparatively investigated the variation in the effect of the NWC transmitter on the plasma number density at the satellite altitude and the plasma temperature in three modes of operation: continuously operating, switching off, and keying operation of the NWC transmitter. They concluded that the average plasma number density at the satellite altitude is essentially independent of the operation of the NWC transmitter. In contrast, the average plasma temperature and the plasma perturbations are closely related to whether the NWC transmitter is switched on.

However, there are still controversies about the propagation properties of VLF after entering the ionosphere. One of the critical issues is whether the signals propagate as ducted or non-ducted. Lehtinen et al. [13,14] concluded that VLF propagates in a whistling mode along the geomagnetic field lines. In contrast, Clilverd et al. [27] argued that whether or not ducted propagation is correlated with the L-shell value, VLF transmitters with $L < 1.5$ are dominated by non-ducted propagation, whereas VLF transmitters with $1.5 < L < 2.5$ are dominated by ducted propagation. Zhang et al. [28] suggested that ducted signals account for only a minority of the propagation of ground-based VLF transmitters in the magnetosphere, while non-ducted modes dominate. Recently, the study by Usanova et al. [29] also found that the signals from VLF transmitters between L-shells of 1.17 and 2.87 are dominated by non-ducted propagation. Therefore, the propagation characteristics of VLF waves in the ionosphere are still worth studying.

In summary, the study of the spatial and temporal distribution of ground-based VLF transmitter radio signals in the ionosphere is crucial for understanding the propagation characteristics of VLF waves penetrating the ionosphere and the perturbation of the ionosphere by solar activities. It is also of great significance for further analysis of the scattering effect of electrons in the radiation belt by VLF waves and the study of sudden space weather events or disasters such as solar flares, lower atmospheric activities (such as lightning and aerosols), and lithospheric activities (such as earthquakes and volcanic eruptions). Therefore, this study investigates the spatial distribution characteristics of the electric field excited in the ionosphere by the NWC transmitter and its seasonal variation using the data from the China Seismo-Electromagnetic Satellite (CSES). Furthermore, it thoroughly analyzes

changes in the location of the peak center of the electric field, providing valuable insights into the propagation characteristics of VLF waves within the ionosphere.

2. Data

VLF transmitters, such as the NWC transmitter located in Australia (21.82° S 114.17° E), play a crucial role in naval communications and are primarily used as naval military radars. The NWC transmitter is a VLF transmitter operating in the Southern Hemisphere with a radiated power of 1000 kW and a radiated signal frequency of 19.8 kHz, with a bandwidth of 300 Hz. It typically operates continuously throughout the week, except for Monday mornings when it is shut down. The transmission method used is minimum frequency shift keying, ensuring stable and consistent operation. The NWC transmitter was active from 2019 to 2021.

The China Seismo-Electromagnetic Satellite was launched in February 2018 with the objective of establishing a space test platform for monitoring various aspects of the global space electromagnetic field, including electromagnetic waves, ionospheric plasma, and high-energy particle precipitation. It serves as a valuable tool for monitoring and forecasting the space environment and conducting scientific research on the Earth system [30]. Operating at an altitude of 507 km and an orbital inclination of 97°, the satellite follows a sun-synchronous orbit, with descending nodes consistently occurring at 14:00 and 02:00 local time. With a revisit cycle of five days, the satellite is capable of continuous detection within latitudes of up to 65° north and south at all times of the day. The satellite operates in two modes: burst and survey. For this study, the electric field power spectral density data in the VLF band from 2019 to 2021 were utilized, obtained in survey mode with a sampling frequency of 50 kHz, a time resolution of 2 s, and a frequency resolution of 24.4 Hz [31,32].

The decision to exclusively utilize nighttime satellite observations in the article stems from the NWC transmitter's location at low latitudes. Daytime satellite observations in equatorial regions often encounter significant noise interference problems. Therefore, to ensure reliable data collection and minimize such interference, this study focused solely on nighttime observations.

3. Spatial and Temporal Distribution of the NWC Transmitter Radio Signals

In order to investigate the spatial distribution of VLF radio signals penetrating the ionosphere, we divided the geographic latitude and longitude into a 1° × 1° grid. Within each grid, we calculated the average value of the electric field power spectral density at the operating frequency of the NWC transmitter. This allowed us to obtain the spatial distribution of the electric field at satellite altitude for the NWC transmitter. Figure 1 illustrates the spatial distribution of the electric field power spectral density radiated by the NWC transmitter in different months, with geographic latitude and longitude. The unit of the electric field power spectral density is expressed in $\lg(\mu\text{V}^2 \cdot \text{m}^{-2} \cdot \text{Hz}^{-1})$. From Figure 1, several key observations can be made: (1) An electric field response occurs over the NWC transmitter, spanning approximately 50° in longitude and 30° in latitude, forming a circular pattern. (2) The center of the electric field signal of the NWC transmitter is shifted to the northwest relative to the ground location of the NWC transmitter. This westward offset in longitude is likely due to the Coriolis force resulting from the rotation of the Earth, as well as the westward drag of aerosols at higher altitudes [33,34]. The northward shift in latitude may be attributed to the propagation of VLF waves aligning with the geomagnetic field [13]. (3) By comparing the power spectrum density distribution of the electric field over the NWC transmitter in December 2019 and June 2020, it is evident that the strength and coverage of the electric field are greater in June than in December. This indicates potential seasonal variations that may influence the phenomenon.

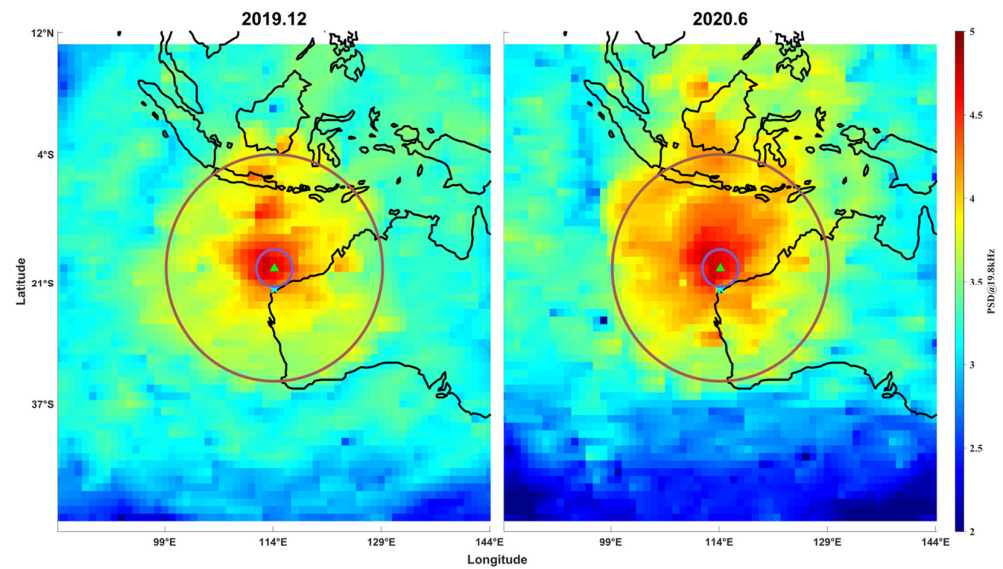


Figure 1. The figure illustrates the spatial distribution of the electric field power spectral density of the NWC transmitter during nighttime in different months, as a function of geographic latitude and longitude. The Northwest Cape (NWC) transmitter is represented by a light blue pentagram, while the position of the NWC transmitter crossing point (which represents the position of the geomagnetic field line at 80 km above the NWC transmitter at satellite altitude) is indicated by a green triangle. The purple circle represents an area with a radius of 2.5° centered on the crossing point, while the brown circle represents an area with a radius of 15° centered on the crossing point.

To further investigate the seasonal variation pattern in the strength of the electric field, we divided the study area into two different sizes. Additionally, considering the close proximity between the center of the electric field and the crossing point (which represents the position of the geomagnetic field line at 80 km above the NWC transmitter at satellite altitude) as depicted in Figure 1, we selected two spatial scales with radii of 15° (shown as brown circles in Figure 1) and 2.5° (shown as purple circles in Figure 1), centered on the crossing point. Subsequently, we conducted a monthly analysis of the electric field strength over a span of three years.

3.1. Seasonal Variation Patterns of the Electric Field Strength

Figure 2 provides the monthly average of the electric field power spectral density in the two study areas from 2019 to 2021. In the 15° radius area, represented by the green curve, a clear seasonal variation pattern is observed. The power spectral density of the electric field reaches its maximum in June, July, and August, corresponding to the winter months in the Southern Hemisphere. Conversely, the minimum occurs in December, January, and February, corresponding to the summer months in the Southern Hemisphere.

This differentiation in strength is due to the energy attenuation of VLF waves in the low ionosphere during their propagation to the top of the ionosphere, with most of the attenuation occurring below 120 km. After penetrating the low ionosphere, VLF waves convert into whistling waves that propagate along the geomagnetic field line with minimal energy decay. The electron density in the low ionosphere is primarily influenced by solar extreme ultraviolet radiation. In summer, when the solar zenith angle is smallest and the solar extreme ultraviolet radiation flux is highest, the degree of ionization of the lower ionosphere increases, leading to a higher electron density. This results in increased energy attenuation of VLF waves penetrating the ionosphere and a decrease in the strength of VLF radio signals observed by satellites. In contrast, during winter, with the largest solar zenith angle and lowest solar extreme ultraviolet radiation flux, the degree of ionization of the lower ionosphere decreases, resulting in less energy attenuation of VLF waves penetrating

the ionosphere. Consequently, the strength of satellite-observed VLF radio signals increases. These findings are consistent with previous studies [19,20,35].

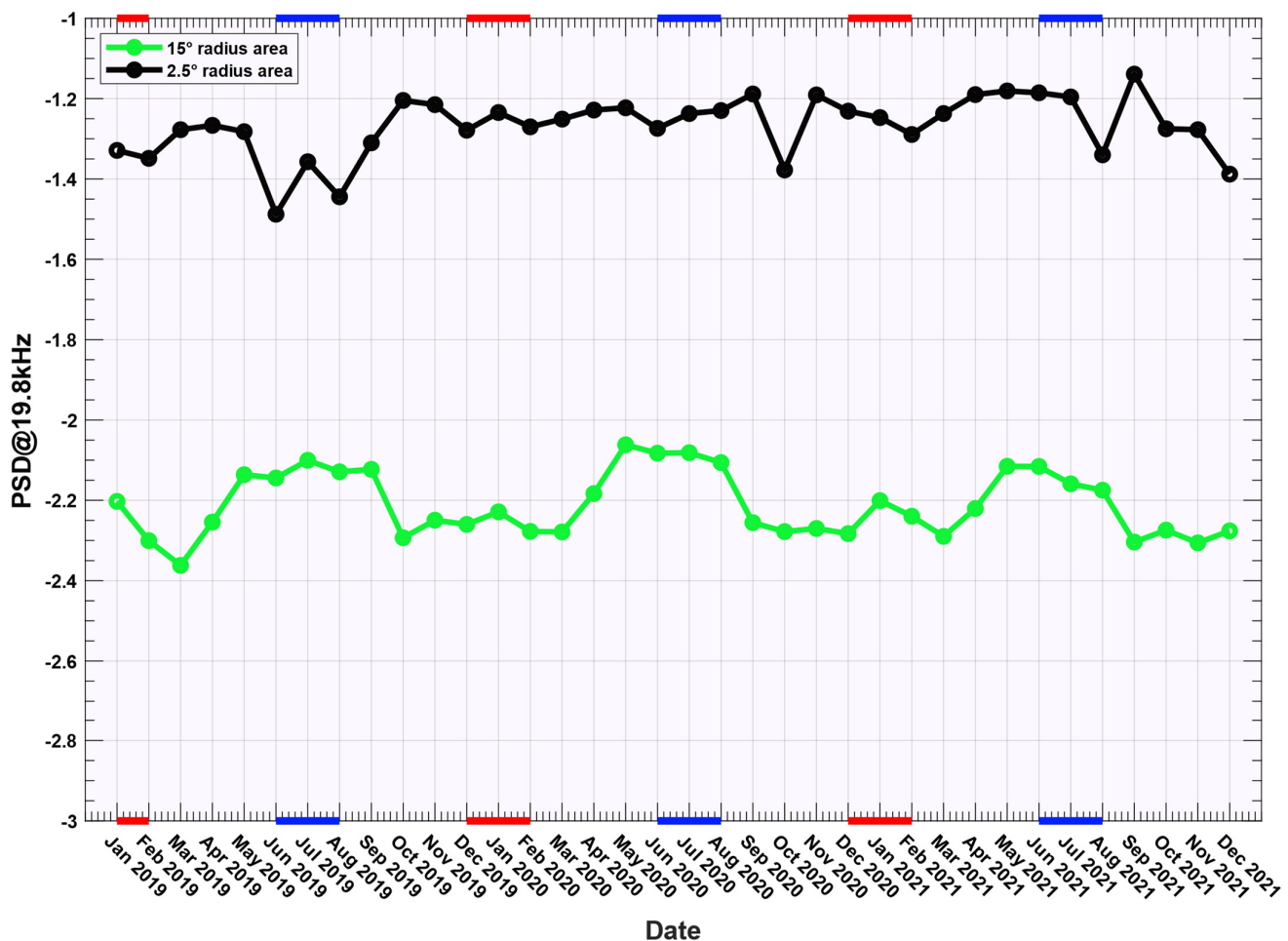


Figure 2. Monthly plots illustrating the mean power spectral density of the electric field of the NWC transmitter at night across various spatial scales. The green curve represents the 15° radius area, while the black curve represents the 2.5° radius area. Additionally, the red straight line denotes summer, and the blue straight line denotes winter.

On the other hand, the black curve depicts the 2.5° radius area, which does not exhibit significant seasonal variations in the electric field power spectral density. This finding aligns with the results reported by Cohen and Inan (2012) [26], who analyzed the strength of the electric field within 150 km centered on the crossing point using the DEMETER satellite. Their findings indicated that the strength of the electric field does not vary with solar activity within this range. There are two possible explanations for the lack of seasonal variation at smaller regional scales. Firstly, the center electric field strength may be too strong to exhibit noticeable seasonal variations. Secondly, the operation of the NWC transmitter may introduce a heating effect in the lower ionosphere, increasing the electron temperature mainly within 250 km [36] and, consequently, decreasing the electron density [12]. This leads to a reduction in the propagation attenuation of VLF within the region, further minimizing the impact of seasonal variations in the electron density in the lower ionosphere. As a result, the electric field power spectral density within the small region over the NWC transmitter exhibits non-seasonal variations.

3.2. Spatial Distribution of the NWC Transmitter Radio Signals

In this section, we aim to delve deeper into the spatial distribution of the NWC transmitter radio signal. To achieve this, we focus on the orbit that is closest to the NWC transmitter (approximately 1.2° west of the transmitter) and its revisited orbit data. Through this investigation, we aim to identify the differences in the spatial distribution of the electric field during the summer and winter seasons. Figure 3a,c,e, respectively, display the latitude-based distribution of electric field power spectral density for the summer months of 2019, 2020, and 2021. Conversely, Figure 3b,d,f, respectively, present the distribution of electric field power spectral density with latitude for the winter months of 2019, 2020, and 2021.

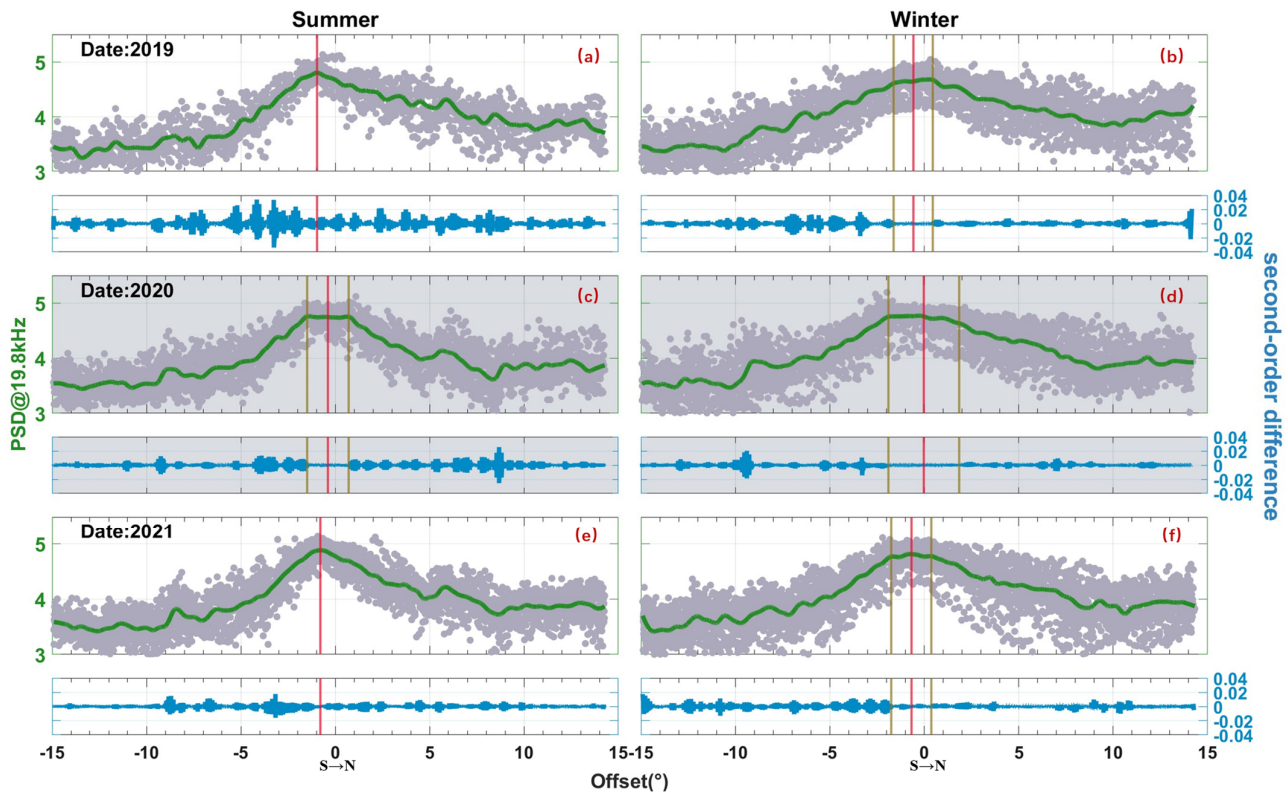


Figure 3. The power spectral density of the electric field is depicted in a latitudinal distribution at various times, along with the second-order difference map of the power spectral density of the electric field (2019 to 2021 are shown in chronological order from top to bottom, with summer and winter from left to right, corresponding to (a–f) in the figure, respectively). The latitudinal distribution is centered on the latitude of the crossing point. The green curve represents the fitted line that corresponds to the scattered data points represented by the grey dots. The blue curve represents the second order difference of the green curve. The red vertical line represents the location of the identified centroid of the electric field, while the brown line depicts the boundary of the identified “platform”.

To analyze the distribution of the electric field relative to the NWC transmitter crossing point, the scattered gray points in the figure represent the power spectral density of all measured data points, corresponding to the latitude difference from the NWC transmitter crossing point. The green curve is a smoothed and fitted curve obtained from the scattered data. From the green fitted curve in Figure 3, several observations can be made: (1) The distribution of the electric field exhibits a north–south asymmetry, with higher strength observed north of the peak compared with the south. The average power spectral density of radio signals in the northern region is approximately $4.2 \lg(\mu\text{V}^2 \cdot \text{m}^{-2} \cdot \text{Hz}^{-1})$, while in the southern region, it is around $3.6 \lg(\mu\text{V}^2 \cdot \text{m}^{-2} \cdot \text{Hz}^{-1})$. (2) A comparison of the latitudinal distribution curves of the electric field strength in different seasons reveals that the curve is

flatter during winter compared with summer. In other words, the decay rate of the electric field with distance is smaller in winter than in summer. (3) Additionally, interference from wave modes mapped from the Earth–ionosphere waveguide is observed near 6° from the NWC transmitter crossing point during the summers of 2020 and 2021 [13,14,37].

Upon analyzing Figure 3b–d,f, a distinct “platform” in the electric field amplitude can be observed within a specific range near the crossing point. This “platform” represents a region where the power spectral density remains relatively constant with distance. To quantify this range, we perform second-order differencing on the green curve in Figure 3, resulting in the blue plot. The start and end locations of these “platforms” are determined using second-order differencing, indicated by the brown vertical lines. Notably, these “platforms” are predominantly observed during the winter season. In winter 2020, the width of the platform is 3.7° , which is significantly broader than in other years. A similar phenomenon occurs in the summer of the same year, albeit with a narrower width compared with winter. This behavior resembles a saturation effect, which typically arises when the electron density in the lower ionosphere is low. During winter nights, when the electron density in the lower ionosphere is relatively lower, the ionospheric energy absorption into the waves becomes negligible, resulting in a more extensive saturation zone. This phenomenon explains the absence of noticeable seasonal variations in the electric field within a 2.5° radius, as mentioned in the previous section, while revealing a seasonal variation pattern within a 15° radius.

Furthermore, we conducted a detailed investigation into the variation in the position of the electric field center. In situations where no “platform” is identified, we directly locate the peak of the green line as the center of the electric field. However, when a “platform” is detected, we consider the center of the “platform” as the position of the electric field center (indicated by the red vertical line). The offsets for the winter and summer seasons of 2019, 2020, and 2021 are illustrated in Figure 4. The electric field center offset displays a noticeable seasonal variation, with a larger offset observed in summer compared with winter. The center shifts toward the north from summer to winter, with an average offset of approximately 0.3° . To examine the variation in the electric field center offset in more detail, we introduce orbit data from the other side as a constraint.

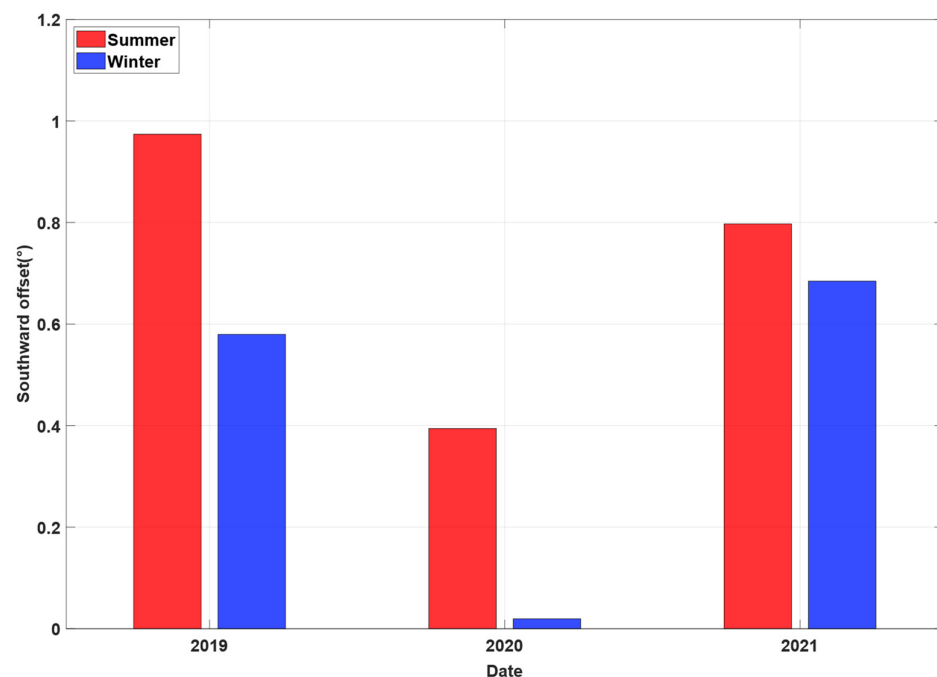


Figure 4. Plot illustrating the latitudinal offset of the electric field center in relation to the crossing point for the NWC transmitter in different years, categorized by seasons.

3.3. Seasonal Variations in the Peak Shifts of the Electric Field Center

In the preceding section, we selected the orbit closest to the NWC transmitter on the western side and examined the spatial distribution of signals in that satellite orbit, leading to the discovery of the “platform”. To determine the shift of the center of the electric field and changes in the size of the “platform”, we employed data from the other side (approximately 3.6° east of the NWC transmitter) as constraints. By comparing the spatial distribution of signals gathered from orbital data on both sides, we can further analyze them.

In Figure 5, the left column displays the distribution of smoothed values of the electric field power spectral density along the latitudinal offset for different orbits (the black line represents the data from the west side of the NWC transmitter, while the green line corresponds to the data from the east side) during different years in the summer season. The middle column pertains to the winter season. Observations from the figure reveal the following: (1) The east orbit never captures the “platform” of the electric field strength observed by the west orbit, as the east orbit does not traverse the region where the electric field “platform” exists, which is characterized by a constant strength regardless of distance. (2) The peak of the electric field power spectral density is more pronounced in the western orbit compared with the eastern orbit, attributed to the proximity of the electric field center to the western orbit. The difference between the power spectral densities of the east and west orbits is less significant in winter than in summer, due to the expanded “platform” during the winter season. (3) The east orbit displays evident seasonal variations, with the peak intensity consistently higher in winter than in summer. Conversely, the west orbit does not exhibit this phenomenon. This observation provides further evidence that the electric field at the NWC transmitter experiences no seasonal variations within a limited region but displays seasonal variations beyond this region.

After incorporating data from the eastern orbit, we were able to determine that the center of the NWC transmitter electric field lies between the eastern and western orbits. To pinpoint the precise location of the center, we made several key determinations. Firstly, based on previous research and Figure 1 of this paper, we assumed that the electric field is a strictly circular region. Secondly, using the nearest track data on the west side in Figure 3, we identified the location of the peak center of the electric field and used the geometric plumbing theorem to determine the line where the center of the circle is located. Thirdly, we determined the radius of the center of the circle by identifying the location of the same electric field power spectral density value for the east and west orbits on the north side (points A and B in the subplots of Figure 5). Finally, we obtained schematic diagrams of the electric field center offset across seasons in each subfigure of Figure 5.

Our findings in Figure 5 indicate the following: (1) When the western orbital data fall within the center of the electric field, the fitted curve exhibits a distinct “platform” as shown in Figure 3. This indicates that the electric field power spectral density remains constant and does not decay with distance inside the center of the electric field. (2) Throughout the transition from summer to winter, the range of the electric field center expands. This expansion is attributed to the decrease in electron density within the low ionosphere due to the weakening of solar radiation during winter. (3) In the Southern Hemisphere, the center of the electric field shifts in a northerly direction from summer to winter, and this seasonal variation in direction may be related to the movement of the sun between the Tropic of Cancer and the Tropic of Capricorn. The sun moves northward from summer to winter, causing the center of the electric field to shift northward. (4) The propagation of the NWC transmitter radio signals within the radiative centers is primarily dominated by ducted signal propagation. However, an exception can be observed during the summer of 2019, when the crossing point falls outside the center of the electric field. This suggests that during this time, the NWC transmitter signal may have been primarily influenced by non-ducted propagation.

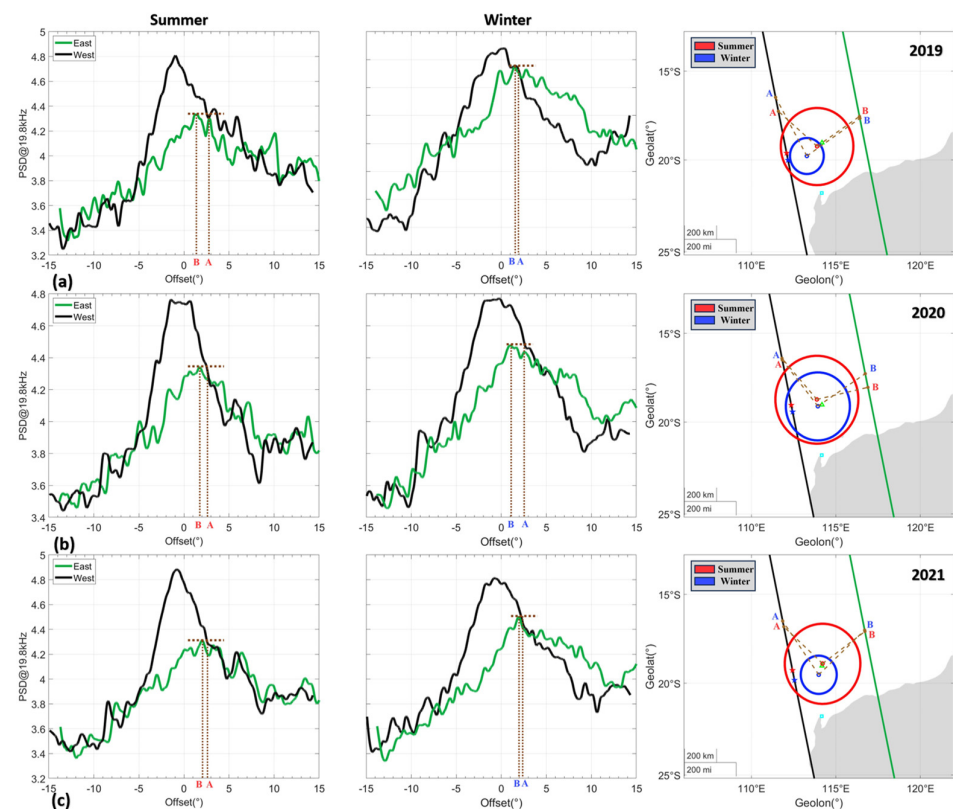


Figure 5. Plots of the latitudinal distribution of the power spectral density of the electric field and the seasonal evolution of the center of the electric field (plots (a–c) are for 2019 to 2021, respectively, and the latitudinal distribution is centered on the latitude of the NWC transmitter crossing point). The green triangles show the position of the crossing point, the light blue squares indicate the position of the NWC transmitter, and the pentagrams correspond to the relative peak positions of the electric field centers in the respective orbits for each season. Points A and B in the figure represent the locations of the same electric field power spectral density values in different orbits.

4. Summary and Conclusions

Due to contamination of the CSES dayside data over the NWC transmitter with a wide bandwidth, this paper focuses solely on the CSES nightside data to examine the spatial and temporal distribution of the NWC transmitter radio signals. While various factors affect the nightside low ionosphere [38], the influence of solar radiation on the nightside, particularly the late-night low ionosphere, remains poorly understood. Previous studies have indicated significant seasonal variations in the D region of the nightside ionosphere [18,19]. Specifically, during winter nights, the ionospheric height reaches its peak, leading to lower electron densities in the D region. This is followed by spring and autumn, with the lowest ionospheric height occurring in summer. Therefore, this paper utilizes data from the CSES during nighttime from 2019 to 2021 to investigate the relationship between the NWC transmitter electric field and solar activity on the night side, as well as its unique spatial and temporal characteristics.

The following main conclusions were drawn from the study:

- (1) Statistical analysis reveals a clear seasonal pattern in the NWC transmitter radio signal within a radius of 15 degrees from the center of the crossing point. The signal is more prominent in June, July, and August (winter) and smaller in December, January, and February (summer). However, no seasonal pattern is observed within a small area of a 2.5-degree radius from the center of the crossing point over the NWC transmitter.
- (2) A “platform” region with a peak center is identified in the electric field over the NWC transmitter. Within this region, the electric field power spectral density does not significantly decay with distance. However, outside of this region, decay with

distance becomes apparent, showing a north–south asymmetry. The average power spectral density of the electric field is stronger in the north than in the south, and the decay rate is slower in the north.

- (3) There is a noticeable northward shift in the peak center of the NWC transmitter electric field from summer to winter. Additionally, during the winter season, we observe an expansion in the range of peak centers of the electric fields.
- (4) Except for the summer of 2019, ducted propagation predominantly occurs in the radiation center over the NWC transmitter. However, during the summer of 2019, non-ducted propagation may dominate the VLF signals in the radiation center over the NWC transmitter.

Author Contributions: Conceptualization, S.Z., L.L. and X.S.; formal analysis, H.C. and L.L.; investigation, S.Z., H.C. and L.L.; methodology, H.C., S.Z. and L.L.; data curation, S.Z. and H.L.; resources, S.Z. and X.S.; supervision, S.Z., X.S. and L.L.; visualization, H.C., S.Z. and L.L.; writing—original draft, H.C., L.L. and S.Z.; and writing—review and editing, H.C., S.Z., L.L. and X.S. All authors have read and agreed to the published version of the manuscript.

Funding: This study is supported by the Specialized Research Fund for State Key Laboratories, National Space Science Center, Chinese Academy of Sciences; Talent startup research grants from National Space Science Center, Chinese Academy of Sciences (Grant Nos. 2023000034, E3RC2TQ4, and E3RC2TQ5); the National Natural Science Foundation of China (Grant No. 41704156); and the China Research Institute of Radiowave Propagation (Research on low ionosphere satellite detection).

Institutional Review Board Statement: Not applicable.

Informed Consent Statement: Not applicable.

Data Availability Statement: Data of the CSES mission can be retrieved from the website (<https://www.leos.ac.cn/#/login?redirect=/dataService/dataDownloadList> (accessed on 1 July 2023)) after registration (<https://www.leos.ac.cn/#/register> (accessed on 1 July 2023)).

Acknowledgments: We would like to express our sincere gratitude to the National Space Science Centre of the Chinese Academy of Sciences (NSSC) for their financial support provided for this work. This work made use of the data from the CSES mission, a project funded by the China National Space Administration (CNSA) and the China Earthquake Administration (CEA). Thanks to the CSES mission team for the data.

Conflicts of Interest: The authors declare no conflict of interest.

References

1. Helliwell, R.A. *Whistlers and Related Ionospheric Phenomena*; Stanford University Press: Stanford, CA, USA, 1965; Volume 11, pp. 563–564.
2. Ni, B.; Huang, H.; Zhang, W.; Gu, X.; Zhao, H.; Li, X.; Baker, D.; Fu, S.; Xiang, Z.; Cao, X. Parametric Sensitivity of the Formation of Reversed Electron Energy Spectrum Caused by Plasmaspheric Hiss. *Geophys. Res. Lett.* **2019**, *46*, 4134–4143. [[CrossRef](#)]
3. Ni, B.; Hua, M.; Zhou, R.; Yi, J.; Fu, S. Competition between Outer Zone Electron Scattering by Plasmaspheric Hiss and Magnetosonic Waves. *Geophys. Res. Lett.* **2017**, *44*, 3465–3474. [[CrossRef](#)]
4. Meredith, N.P.; Horne, R.B.; Clilverd, M.A.; Ross, J.P.J. An Investigation of VLF Transmitter Wave Power in the Inner Radiation Belt and Slot Region. *J. Geophys. Res. Space Phys.* **2019**, *124*, 5246–5259. [[CrossRef](#)]
5. Cao, X.; Ni, B.; Summers, D.; Fu, S.; Gu, X.; Shi, R. Hot Plasma Effects on the Pitch-Angle Scattering Rates of Radiation Belt Electrons Due to Plasmaspheric Hiss. *Astrophys. J.* **2020**, *896*, 118. [[CrossRef](#)]
6. Inan, U.S.; Chang, H.C.; Helliwell, R.A. Electron Precipitation Zones around Major Ground-Based VLF Signal Sources. *J. Geophys. Res. Space Phys.* **1984**, *89*, 2891–2906. [[CrossRef](#)]
7. Inan, U.S.; Chang, H.C.; Helliwell, R.A.; Imhof, W.L.; Reagan, J.B.; Walt, M. Precipitation of Radiation Belt Electrons by Man-Made Waves: A Comparison between Theory and Measurement. *J. Geophys. Res. Space Phys.* **1985**, *90*, 359–369. [[CrossRef](#)]
8. Clilverd, M.A.; Horne, R.B. Ground-Based Evidence of Latitude-Dependent Cyclotron Absorption of Whistler Mode Signals Originating from VLF Transmitters. *J. Geophys. Res. Space Phys.* **1996**, *101*, 2355–2367. [[CrossRef](#)]
9. Gamble, R.J.; Rodger, C.J.; Clilverd, M.A.; Sauvaud, J.-A.; Thomson, N.R.; Stewart, S.L.; McCormick, R.J.; Parrot, M.; Berthelier, J.-J. Radiation Belt Electron Precipitation by Man-Made VLF Transmissions. *J. Geophys. Res. Space Phys.* **2008**, *113*, A10211. [[CrossRef](#)]
10. Selesnick, R.S.; Albert, J.M.; Starks, M.J. Influence of a Ground-Based VLF Radio Transmitter on the Inner Electron Radiation Belt. *J. Geophys. Res. Space Phys.* **2013**, *118*, 628–635. [[CrossRef](#)]

11. Cunningham, G.S.; Botek, E.; Pierrard, V.; Cully, C.; Ripoll, J.-F. Observation of High-Energy Electrons Precipitated by NWC Transmitter From PROBA-V Low-Earth Orbit Satellite. *Geophys. Res. Lett.* **2020**, *47*, e2020GL089077. [[CrossRef](#)]
12. Němec, F.; Pekař, J.; Parrot, M. NWC Transmitter Effects on the Nightside Upper Ionosphere Observed by a Low-Altitude Satellite. *J. Geophys. Res. Space Phys.* **2020**, *125*, e2020JA028660. [[CrossRef](#)]
13. Lehtinen, N.G.; Inan, U.S. Full-Wave Modeling of Transionospheric Propagation of VLF Waves. *Geophys. Res. Lett.* **2009**, *36*, L03104. [[CrossRef](#)]
14. Lehtinen, N.G.; Inan, U.S. Radiation of ELF/VLF Waves by Harmonically Varying Currents into a Stratified Ionosphere with Application to Radiation by a Modulated Electrojet. *J. Geophys. Res. Space Phys.* **2008**, *113*, A06301. [[CrossRef](#)]
15. Zhao, S.; Liao, L.; Zhang, X. Trans-ionospheric VLF wave power absorption of terrestrial VLF signal. *Chin. J. Geophys.* **2017**, *60*, 3004–3014. (In Chinese)
16. Zhao, S.; Zhou, C.; Shen, X.; Zhima, Z. Investigation of VLF Transmitter Signals in the Ionosphere by ZH-1 Observations and Full-Wave Simulation. *J. Geophys. Res. Space Phys.* **2019**, *124*, 4697–4709. [[CrossRef](#)]
17. Schmölter, E.; von Savigny, C. Solar Activity Driven 27-Day Signatures in Ionospheric Electron and Molecular Oxygen Densities. *J. Geophys. Res. Space Phys.* **2022**, *127*, e2022JA030671. [[CrossRef](#)]
18. Richardson, D.K.; Cohen, M.B. Seasonal Variation of the D-Region Ionosphere: Very Low Frequency (VLF) and Machine Learning Models. *J. Geophys. Res. Space Phys.* **2021**, *126*, e2021JA029689. [[CrossRef](#)]
19. Maurya, A.K.; Veenadhari, B.; Singh, R.; Kumar, S.; Cohen, M.B.; Selvakumaran, R.; Gokani, S.; Pant, P.; Singh, A.K.; Inan, U.S. Nighttime D Region Electron Density Measurements from ELF-VLF Tweek Radio Atmospherics Recorded at Low Latitudes. *J. Geophys. Res. Space Phys.* **2012**, *117*, A11308. [[CrossRef](#)]
20. Zhao, S.; Liao, L.; Shen, X.; Lu, H.; Zhima, Z.; Huang, J.; Zhou, C. CSES Satellite Observations of 50 Hz Power Line Radiation Over Mainland China and Its Response to COVID-19. *J. Geophys. Res.* **2022**, *127*, e2022JA030693. [[CrossRef](#)]
21. Gu, X.; Wang, Q.; Ni, B.; Xu, W.; Wang, S.; Yi, J.; Hu, Z.; Li, B.; He, F.; Chen, X.; et al. First Results of the Wave Measurements by the WHU VLF Wave Detection System at the Chinese Great Wall Station in Antarctica. *J. Geophys. Res. Space Phys.* **2022**, *127*, e2022JA030784. [[CrossRef](#)]
22. Šulić, D.M.; Srećković, V.A.; Mihajlov, A.A. A Study of VLF Signals Variations Associated with the Changes of Ionization Level in the D-Region in Consequence of Solar Conditions. *Adv. Space Res.* **2016**, *57*, 1029–1043. [[CrossRef](#)]
23. Marshall, R.A.; Inan, U.S. Two-Dimensional Frequency Domain Modeling of Lightning EMP-Induced Perturbations to VLF Transmitter Signals: MODELING VLF TRANSMITTER PERTURBATIONS. *J. Geophys. Res. Space Phys.* **2010**, *115*, A00E29. [[CrossRef](#)]
24. Zhao, S.; Shen, X.; Liao, L.; Zhima, Z.; Zhou, C.; Wang, Z.; Cui, J.; Lu, H. Investigation of Precursors in VLF Subionospheric Signals Related to Strong Earthquakes ($M > 7$) in Western China and Possible Explanations. *Remote Sens.* **2020**, *12*, 3563. [[CrossRef](#)]
25. Zhang, X.; Wang, Y.; Boudjada, M.Y.; Liu, J.; Magnes, W.; Zhou, Y.; Du, X. Multi-Experiment Observations of Ionospheric Disturbances as Precursory Effects of the Indonesian Ms6.9 Earthquake on August 05, 2018. *Remote Sens.* **2020**, *12*, 4050. [[CrossRef](#)]
26. Cohen, M.B.; Inan, U.S. Terrestrial VLF Transmitter Injection into the Magnetosphere: VLF TRANSMITTER INJECTION. *J. Geophys. Res. Space Phys.* **2012**, *117*, A08310. [[CrossRef](#)]
27. Clilverd, M.A.; Rodger, C.J.; Gamble, R.; Meredith, N.P.; Parrot, M.; Berthelier, J.-J.; Thomson, N.R. Ground-Based Transmitter Signals Observed from Space: Ducted or Nonducted? *J. Geophys. Res. Space Phys.* **2008**, *113*, A04211. [[CrossRef](#)]
28. Zhang, Z.; Chen, L.; Li, X.; Xia, Z.; Heelis, R.A.; Horne, R.B. Observed Propagation Route of VLF Transmitter Signals in the Magnetosphere: GROUND TRANSMITTER PROPAGATION. *J. Geophys. Res. Space Phys.* **2018**, *123*, 5528–5537. [[CrossRef](#)]
29. Usanova, M.E.; Reid, R.A.; Xu, W.; Marshall, R.A.; Starks, M.J.; Wilson, G.R. Using VLF Transmitter Signals at LEO for Plasmasphere Model Validation. *J. Geophys. Res. Space Phys.* **2022**, *127*, e2022JA030345. [[CrossRef](#)]
30. Shen, X.; Zong, Q.-G.; Zhang, X. Introduction to Special Section on the China Seismo-Electromagnetic Satellite and Initial Results. *Earth Planet. Phys.* **2018**, *2*, 439–443. [[CrossRef](#)]
31. Zhima, Z.; Zhou, B.; Zhao, S.; Wang, Q.; Huang, J.; Zeng, L.; Lei, J.; Chen, Y.; Li, C.; Yang, D.; et al. Cross-Calibration on the Electromagnetic Field Detection Payloads of the China Seismo-Electromagnetic Satellite. *Sci. China Technol. Sci.* **2022**, *65*, 1415–1426. [[CrossRef](#)]
32. Huang, J.; Lei, J.; Li, S.; Zeren, Z.; Li, C.; Zhu, X.; Yu, W. The Electric Field Detector (EFD) Onboard the ZH-1 Satellite and First Observational Results. *Earth Planet. Phys.* **2018**, *2*, 469–478. [[CrossRef](#)]
33. Pulnits, S.; Ouzounov, D. Lithosphere–Atmosphere–Ionosphere Coupling (LAIC) Model—An Unified Concept for Earthquake Precursors Validation. *J. Asian Earth Sci.* **2011**, *41*, 371–382. [[CrossRef](#)]
34. Němec, F.; Santolík, O.; Parrot, M. Decrease of Intensity of ELF/VLF Waves Observed in the Upper Ionosphere Close to Earthquakes: A Statistical Study: WAVE ATTENUATION CLOSE TO EARTHQUAKES. *J. Geophys. Res. Space Phys.* **2009**, *114*, A04303. [[CrossRef](#)]
35. Xiang, Z.; Lin, X.; Chen, W.; Wang, Y.; Lu, P.; Gong, W.; Ma, W.; Hua, M.; Liu, Y. Global morphology of NWC and NAA very-low-frequency transmitter signals in the inner magnetosphere, A survey using Van Allen Probes EMFISIS measurements. *Chin. J. Geophys.* **2021**, *64*, 3860–3869. (In Chinese)

36. Graf, K.L.; Lehtinen, N.G.; Spasojevic, M.; Cohen, M.B.; Marshall, R.A.; Inan, U.S. Analysis of Experimentally Validated Trans-Ionospheric Attenuation Estimates of VLF Signals. *J. Geophys. Res. Space Phys.* **2013**, *118*, 2708–2720. [[CrossRef](#)]
37. Zhang, S.; Chen, E.; Wang, Y.; Pan, W.; Zhang, H. Estimation of VLF amplitude standard deviation in multimode interference region. *Chin. J. Radio Sci.* **2011**, *26*, 286–290.
38. Han, F.; Cummer, S.A. Midlatitude Nighttime D Region Ionosphere Variability on Hourly to Monthly Time Scales. *J. Geophys. Res. Space Phys.* **2010**, *115*, A09323. [[CrossRef](#)]

Disclaimer/Publisher’s Note: The statements, opinions and data contained in all publications are solely those of the individual author(s) and contributor(s) and not of MDPI and/or the editor(s). MDPI and/or the editor(s) disclaim responsibility for any injury to people or property resulting from any ideas, methods, instructions or products referred to in the content.